

# A RELATION BETWEEN SUPERMASSIVE BLACK HOLE MASS AND QUASAR METALLICITY?

CRAIG WARNER<sup>1</sup>, FRED HAMANN<sup>1</sup>, AND MATTHIAS DIETRICH<sup>2</sup>  
*Draft version October 9, 2018*

## ABSTRACT

We analyze spectra for a large sample of 578 Active Galactic Nuclei to examine the relationships between broad emission line properties and central supermassive black hole (SMBH) mass. We estimate SMBH masses by applying the virial theorem to the C IV  $\lambda 1549$  broad emission line. Although the FWHMs of C IV and  $H\beta$  appear nearly unrelated in individual objects, these FWHMs are well correlated when averaged over sub-samples in our database. Therefore, the lines are equally valid indicators of the average SMBH mass in quasar samples. Our sample spans five orders of magnitude in SMBH mass, six orders of magnitude in luminosity, and a redshift range from  $0 \leq z \leq 5$ . Most lines diminish in equivalent width with increasing black hole mass (the usual “Baldwin Effect”) and there are no trends with redshift. Recent studies indicate that there is a relationship between SMBH mass and the overall bulge/spheroidal component mass of the surrounding galaxy. This relation, together with the well-known mass-metallicity relationship among galaxies, predicts a relationship between SMBH mass and quasar metallicity. We estimate the metallicity in the broad emission line region by comparing several line ratios involving nitrogen to theoretical predictions. We find that the data are consistent with a trend between SMBH mass and metallicity, with some line ratios indicating a very strong trend, but the uncertainties in several other important line ratios are too large to confirm or test this correlation.

*Subject headings:* galaxies: active—quasars: emission lines—galaxies: formation

## 1. INTRODUCTION

Supermassive black holes (SMBHs) are believed to drive the tremendous energy output of quasars, and more generally, active galactic nuclei (AGNs). Recent studies have shown that the centers of all massive galaxies today harbor SMBHs (Gebhardt et al. 2000a; Ferrarese & Merritt 2002). Moreover, the mass of the black hole scales directly with the mass of the host galaxy, or more specifically, the mass of the host galaxy’s bulge or spheroidal component. The early results were based on a correlation between SMBH mass and bulge luminosity,  $L_{\text{bulge}}$  (Magorrian et al. 1998; Laor 1998; Wandel 1999), which showed a large scatter, as much as two orders of magnitude in SMBH mass (Ferrarese & Merritt 2000). Subsequent studies focused on the relationship between the masses of SMBHs and the velocity dispersions,  $\sigma$ , of their host bulges or spheroids. This relation shows considerably less scatter than the  $M_{\text{SMBH}} - L_{\text{bulge}}$  relation (Ferrarese & Merritt 2000; Gebhardt et al. 2000a; Merritt & Ferrarese 2001; Tremaine et al. 2002). There is also no significant difference between the relationships measured for active and quiescent galaxies (Gebhardt et al. 2000b; Ferrarese et al. 2001). Recently, SMBH mass has also been shown to correlate strongly with the global structure of ellipticals and bulges (e.g. more centrally concentrated bulges have more massive SMBHs). This relationship is as strong as the  $M_{\text{SMBH}} - \sigma$  relationship with comparable scatter (Graham et al. 2001; Erwin et al. 2002). Studies that carefully model the bulge light profiles of disk galaxies and thereby obtain more accurate values of  $L_{\text{bulge}}$  also show less scatter in  $M_{\text{SMBH}} - L_{\text{bulge}}$ , similar to that in the  $M_{\text{SMBH}} - \sigma$  relationship (McLure & Dunlop 2002; Erwin et al. 2002;

Bettoni et al. 2003).

The overall mass of a galaxy is also known to correlate with its metallicity (Faber 1973; Zaritsky et al. 1994; Jablonka et al. 1996; Trager et al. 2000). This relationship is generally understood in terms of the gravitational binding energy. More massive galaxies have deeper potential wells, making it harder for supernovae and stellar winds to blow matter out of the region. Therefore, the gas remains in the galaxy longer, where it is further reprocessed by stars, leading to higher metallicities. This mass-metallicity relationship, combined with the relationship between SMBH mass and galaxy mass, suggests that there should be a relationship between SMBH mass and the metallicity of the gas clouds surrounding quasars (Hamann & Ferland 1993).

The metallicity of the gas in the broad emission line region (BLR) of quasars can be estimated by analyzing prominent emission lines. BLR metallicities should be representative of the gas in the central regions of galaxies if the BLR was enriched by stars in those environments. Previous studies have demonstrated that we cannot simply examine ratios of strong metal to hydrogen lines, such as C IV  $\lambda 1549 / \text{Ly}\alpha$ , to measure the C/H abundance. This is because strong collisionally excited lines like C IV play an important role in cooling the gas. Increasing the metallicity and thus C/H leads to lower gas temperatures and an almost constant C IV /  $\text{Ly}\alpha$  ratio (Hamann & Ferland 1999). The best abundance diagnostics for the BLR involve ratios of lines that are i) not important in the cooling, and ii) have similar excitation/emission requirements (Hamann et al. 2002). Ratios of emission lines involving nitrogen, N, are especially valuable in determin-

<sup>1</sup> Department of Astronomy, University of Florida, 211 Bryant Space Science Center, Gainesville, FL 32611-2055, E-mail: warner@astro.ufl.edu, hamann@astro.ufl.edu

<sup>2</sup> Department of Physics and Astronomy, Georgia State University, Atlanta, Georgia 30303

ing the metallicity,  $Z$ , because of the expected “secondary” N production via the CNO cycle of nucleosynthesis in stars (Shields 1976; Hamann & Ferland 1992, 1993, 1999; Ferland et al. 1996; Hamann et al. 2002). In the CNO cycle, nitrogen is produced from existing carbon and oxygen. The nitrogen abundance should therefore scale roughly as  $N/H \propto Z^2$  or  $N/O \propto O/H \propto Z$  (Tinsley 1980), providing a sensitive metallicity diagnostic even when direct measures of  $Z = O/H$  are not available. Observations of H II regions indicate that secondary nitrogen production and  $N/O \propto O/H$  scaling dominate for  $Z \gtrsim 0.2 - 0.3 Z_{\odot}$  (van Zee et al. 1998; Pettini et al. 2002).

Some other studies suggest that there can be significant departures from the simple  $N/O \propto O/H$  relationship owing to time-dependent or perhaps metallicity-dependent yields of N, O, and C (eg. Henry et al. 2000). These effects are often invoked to explain the observed object-to-object scatter in  $N/O$  versus  $O/H$ . However, there is a general consensus that large (solar or higher)  $N/O$  ratios indicate large (solar or higher) metallicities. Moreover, the most homogeneous and therefore most reliable H II region data (Pilyugin et al. 2002; Pettini et al. 2002) indicate that the scatter in  $N/O$  decreases and the validity of  $N/O \propto O/H$  improves in the regime of roughly solar or higher metallicities. This is the regime of the gas near quasars, based on studies of both their broad emission and intrinsic narrow absorption lines (Constantin et al. 2001; Dietrich et al. 1999, 2003a; Hamann 1997; Hamann & Ferland 1999; Hamann et al. 2002; Osmer et al. 1994; Petitjean et al. 1994; Warner et al. 2002). In this paper, we simply assume that  $N/O \propto O/H$  applies. We also note that our analysis of composite quasar spectra naturally averages over object-to-object variations. Any metallicity trends that we infer from the emission line ratios depend on this assumption of  $N/O \propto O/H$  in addition to measurement and photoionization modeling uncertainties.

We have collected spectra of over 800 “Type 1” AGNs (quasars and Seyfert 1 galaxies) from the HST archives and various ground-based observing programs to examine trends in their emission line properties (Dietrich et al. 2002). 578 of these spectra span the rest-frame UV wavelengths needed for this study. We compute five composite quasar spectra from this sample, representing different intervals in SMBH mass from  $10^6$  to  $10^{10} M_{\odot}$ . We present measurements of the emission lines in these composite spectra and investigate the relationship between SMBH mass and the metallicity of the BLR gas.

## 2. SMBH MASS DETERMINATIONS

We estimated black hole masses by applying the virial theorem,  $M_{\text{SMBH}} = rv^2/G$ , to the line-emitting gas, where  $v$  is the velocity dispersion and  $r$  is the radial distance away from the SMBH (Peterson & Wandel 2000). The relationship between  $v$  and the FWHM of the broad emission line profile depends on the kinematics and geometry, but can be expressed as  $v = k \times \text{FWHM}$ , where  $k$  is a factor on the order of unity (McLure & Dunlop 2001; Vestergaard 2002). Kaspi et al. (2000) express the SMBH mass as

$$M = 1.464 \times 10^5 M_{\odot} \left( \frac{R_{\text{BLR}}}{\text{lt} - \text{days}} \right) \left( \frac{\text{FWHM}}{10^3 \text{ km s}^{-1}} \right)^2 \quad (1)$$

FWHM applies to the broad emission line profile, and  $R_{\text{BLR}}$  is the radial distance between the BLR and the cen-

tral mass/continuum source. Equation (1) assumes the gas in the BLR is gravitationally bound and BLR velocities are random. The exact geometry and kinematics are still debated (e.g. McLure & Dunlop 2001), but are unknown, so we take this approach of random velocities ( $k = \sqrt{3}/2$ ) because it is the most basic and allows for comparison with most other work. Any offset in mass due to different geometric or kinematic assumptions would only affect the absolute SMBH masses and not any trends derived between metallicity and SMBH mass. We estimate  $R_{\text{BLR}}$  based on the observed relation between  $R_{\text{BLR}}$  for a particular line and the continuum luminosity (Kaspi et al. 2000; Vestergaard 2002; Wandel et al. 1999). A particular line must be specified because reverberation studies have shown that the BLR is radially stratified, such that higher ionization lines tend to form closer to the central engine than lower ionization lines (Peterson 1993). Kaspi et al. (2000) find

$$R_{\text{BLR}}(H\beta) = (32.9_{-1.9}^{+2.0}) \left[ \frac{\lambda L_{\lambda}(5100\text{\AA})}{10^{44} \text{ ergs s}^{-1}} \right]^{0.700 \pm 0.033} \text{ lt} - \text{days} \quad (2)$$

where  $R_{\text{BLR}}(H\beta)$  is the radial distance between the central continuum source and the  $H\beta$  emission line region and  $\lambda L_{\lambda}(5100\text{\AA})$  is the continuum luminosity at 5100 Å in the AGN rest frame. We choose to use the C IV  $\lambda 1549$  emission line instead of  $H\beta$  to estimate the SMBH mass because it is more readily observed across the entire redshift range from  $z \sim 0$  to  $z \sim 5$ . C IV may in fact yield a better estimate of SMBH mass than  $H\beta$  because  $H\beta$  can include a narrow line component that forms in a different region and thus must be subtracted before measuring the FWHM. C IV has no such narrow component (Wills et al. 1993, Vestergaard 2002). It has recently been suggested that Mg II  $\lambda 2798$  may be a better indicator of SMBH mass than C IV (McLure & Jarvis 2002). However, C IV is observable over a wider range of redshifts and is clearly the best choice among UV lines at shorter wavelengths. Significant blending effects are much less common for C IV than other strong lines in the rest-frame UV spectrum and absorption effects are much less common for C IV than for Ly $\alpha$  (Vestergaard 2002).

Reverberation studies indicate that the size of the broad emission line region for C IV is about half that of  $H\beta$  (Stirpe et al. 1994; Korista et al. 1995; Peterson 1997; Peterson & Wandel 1999). We modify Equation (2) to account for this and we use a powerlaw of the form  $F_{\nu} \propto \nu^{\alpha}$  with  $\alpha = -0.4$  to estimate a conversion between the continuum luminosity at 5100 Å and 1450 Å. We select  $\alpha = -0.4$  based on average quasar spectra from Brotherton et al. (2001), Vanden Berk et al. (2001), and Dietrich et al. (2002). This yields

$$R_{\text{BLR}}(\text{CIV}) = 9.7 \left[ \frac{\lambda L_{\lambda}(1450\text{\AA})}{10^{44} \text{ ergs s}^{-1}} \right]^{0.7} \text{ lt} - \text{days} \quad (3)$$

Vestergaard (2002) finds that this technique of using the continuum luminosity and the FWHM of C IV yields an estimate of the central black hole mass that has a  $1\sigma$  uncertainty of a factor of three when compared to reverberation mapping studies that use  $H\beta$  to estimate SMBH masses. From Equations (1) and (3), we obtain

$$M = 1.4 \times 10^6 M_{\odot} \left( \frac{\text{FWHM}(\text{CIV})}{10^3 \text{ km s}^{-1}} \right)^2 \left( \frac{\lambda L_{\lambda}(1450\text{\AA})}{10^{44} \text{ ergs s}^{-1}} \right)^{0.7} \quad (4)$$

This is essentially the same as (within 10% of) the mass relationship derived by Vestergaard using C IV and  $\lambda L_\lambda(1350\text{\AA})$  (For this comparison, we again assume the powerlaw index,  $\alpha = -0.4$  between 1450 and 1350  $\text{\AA}$ .) The difference of  $\sim 10\%$  between the two formulae is negligible compared to the  $1\sigma$  uncertainty of a factor of three. See also Netzer (2003) and Corbett et al. (2003) for further discussion of the uncertainties.

While multi-epoch spectra are preferable (to average over variabilities), single-epoch spectra may be used if the signal-to-noise ratio is high enough because the FWHM of single-epoch spectra are generally consistent with the FWHMs of the mean and rms spectra obtained from multi-epoch observations (Vestergaard 2002). It is important to accurately measure the FWHM because the uncertainties in SMBH mass are dominated by the uncertainties in the FWHM. Our composite spectra are each made up of single-epoch observations of multiple quasars and therefore should be approximately equivalent to multi-epoch observations of the same sources.

### 3. DATA & ANALYSIS

We have compiled a sample of more than 800 quasar spectra, spanning a redshift range from  $0 \lesssim z \lesssim 5$  and six orders of magnitude in intrinsic luminosity. The spectra were obtained by several groups using various ground-based instruments, as well as the *International Ultraviolet Explorer (IUE)* and the *Hubble Space Telescope (HST)*. One unique aspect of this sample is that it contains new observations of faint quasars at redshift  $z > 2.5$  (Dietrich et al. 2002). Thus we can avoid to some degree the bias toward higher luminosities at higher redshifts that affects other magnitude-limited samples. 578 of the spectra have UV wavelength coverage that encompasses the range  $950 \lesssim \lambda \lesssim 2050 \text{\AA}$ . Each spectrum was transformed to the rest-frame using a redshift measured from the centroid of the upper 50% of the C IV  $\lambda 1549$  profile. See Dietrich et al. (2002) and Dietrich et al. (2003, in prep) for more details on the AGN sample and how luminosities were obtained. Throughout this paper, we use the cosmological parameters  $H_0 = 65 \text{ km s}^{-1} \text{ Mpc}^{-1}$ ,  $\Omega_M = 0.3$ , and  $\Omega_\Lambda = 0$  (Carroll, Press, & Turner 1992). We used radio flux densities given in Véron-Cetty & Véron (2001) to determine the radio loudness for the quasars.

We use an automated program to estimate the FWHM of C IV in each spectrum. The program averages over noise by applying a smoothing routine that calculates the median of each five-pixel interval. It then fits a local linear continuum (constrained by the flux in 25  $\text{\AA}$  wide intervals centered around 1442.5  $\text{\AA}$  and 1712.5  $\text{\AA}$ ) around C IV, measures the peak flux of the emission line (of the smoothed spectrum), and uses those to estimate the FWHM of the line. Comparisons between the FWHMs estimated by the program and those measured manually indicate an error of  $\lesssim 10\%$  in the estimates. Lines containing significant absorption are flagged by the program and their FWHMs are estimated manually (by manually interpolating across the absorption feature). We use the FWHM of C IV and the continuum luminosity,  $\lambda L_\lambda(1450\text{\AA})$  to estimate the central SMBH mass of each quasar based on

Equation (4).

We then sorted the quasars by SMBH mass into five bins:  $10^6 - 10^7 M_\odot$ ,  $10^7 - 10^8 M_\odot$ ,  $10^8 - 10^9 M_\odot$ ,  $10^9 - 10^{10} M_\odot$ , and  $> 10^{10} M_\odot$ , and computed five composite spectra. Each composite spectrum is the average of all the quasar spectra in a bin (see Table 1 for data about each composite spectrum, including the powerlaw index,  $\alpha$ , of the continuum fit, the number of objects contributing to the composite at and FWHM of C IV and  $H\beta$ , continuum luminosity, and mean SMBH mass). Calculating composite spectra increases the signal-to-noise ratio significantly, making it easier to measure weaker emission lines that may be lost in the noise in individual spectra.

Since narrow absorption features may influence the emission line profiles in composite spectra, we developed a method to detect strong narrow absorption features that exclude the contaminated spectral region of individual spectra from the calculation of the composite spectrum. The procedure is roughly as follows (see Dietrich et al. 2002 for more details). First, a preliminary mean spectrum is calculated from all of the spectra in a given mass bin. Each individual spectrum is then divided by this preliminary mean to derive a ratio spectrum. The ratio spectrum is smoothed with a running boxcar function, which provides in addition to the smoothed ratio also a root-mean-square (rms) value for each wavelength box. A narrow absorption line will cause a sharp increase in the rms spectrum. The contaminated spectral regions of individual spectra, identified by these rms spikes, are excluded from the calculation of the final composite spectra, and no interpolation has been applied (Dietrich et al. 2002).

We next corrected each composite spectrum for strong iron emission lines. To get a first estimate of the contribution of Fe emission, we used the empirical Fe emission template that was carefully extracted from I Zw 1 by Vestergaard & Wilkes (2001), which they very kindly provided for this study. The template is mostly Fe II emission but contains some Fe III emission as well. We have modified this Fe emission template into the UV range  $\lambda\lambda 1200 - 1540 \text{\AA}$  in accordance with photoionization model calculations presented by Verner et al. (1999). Based on our analysis of quasar composite spectra (Dietrich et al. 2002), we found that the strength of Fe line emission in the wavelength range  $\lambda\lambda 1420 - 1470 \text{\AA}$  is equal to  $\sim 2\%$  of the integrated *pseudo continuum* flux in this wavelength range (Dietrich et al. 2002). Fe contributions vary for other wavelength ranges, but we scale the entire template to match the 2% contribution in the range  $1420 - 1470 \text{\AA}$ . This estimate of a 2% contribution is conservatively low to avoid over-subtraction of the Fe emission template. The spectral width of the Fe emission features was adjusted to a width corresponding to the FWHM of the C IV  $\lambda 1549$  emission line profile of each quasar. The appropriated scaled Fe emission template was subtracted from the corresponding composite spectrum. In spite of its small contribution, the estimate of the Fe line emission improves particularly the measurements of N III]  $\lambda 1750$  and lines such as He II  $\lambda 1640$  near an unidentified  $\lambda 1600 \text{\AA}$  emission feature (Laor et al. 1994; Vestergaard & Wilkes 2001).

We used the task NFIT1D in the IRAF<sup>3</sup> software pack-

<sup>3</sup> The Image Reduction and Analysis Facility (IRAF) is distributed by the National Optical Astronomy Observatories, which is operated by the Association of Universities for Research in Astronomy, Inc. (USRA), under cooperative agreement with the National Science Foundation.

age to fit the continuum of each Fe-subtracted spectrum with a powerlaw of the form  $F_\nu \propto \nu^\alpha$ . The fits were constrained by the flux in wavelength intervals between the emission lines, namely in 25 Å wide windows centered at 1460 Å, 1770 Å, and 2000 Å. The spectral indices overall differ from  $\alpha = -0.4$  because the powerlaw fit is to a narrower wavelength range than, for example, Dietrich et al. (2002) or Vanden Berk et al. (2001). However, there is a significant trend for steeper (softer) UV spectra in the low-mass sources (see Table 1). Figures 1 and 2 show the final Fe II-subtracted composite spectra normalized by the continuum fits.

To measure the broad emission lines, we use the spectral fitting routine SPECFIT (Kriss 1994), which employs  $\chi^2$  minimization. We fit each line with one or more Gaussian profiles, with the understanding that each individual Gaussian component may have no physical meaning by itself. Our goal in fitting the lines is simply to measure the total line strengths free of blends. Our strategy is to obtain the best fit with the least number of free parameters and, when necessary, to use the profile of strong unblended lines, such as C IV, to constrain the fits to weaker or more blended lines. Figure 3 shows an example of these fits. The Appendix provides details of our fitting procedure for different lines/blends. Table 2 lists the resulting line fluxes relative to  $\text{Ly}\alpha$ , plus the rest-frame equivalent widths (REWs) as measured above the fitted continuum, and the FWHM of each line. The fluxes, REWs, and FWHMs given in Table 2 are from the total fitted profiles, which can include several multiplet components and up to three Gaussian profiles per component (as described in the Appendix).

The primary uncertainty in our flux measurements is the continuum location. We estimate the  $1\sigma$  standard deviation of our measurements of the fluxes of C IV and  $\text{Ly}\alpha$  to be  $\lesssim 10\%$  based on repeated estimates with the continuum drawn at different levels. By the same method, we estimate the uncertainty in N V, N III], He II, O III], and other weaker lines to be  $\sim 10\text{--}20\%$ . These estimates do not include the uncertainties due to line blending, which can be important for some of the weak lines and for N V in the wing of  $\text{Ly}\alpha$ . The blending and continuum placement uncertainties are both greater for the higher mass spectra because of the broader profiles and generally lower REWs.

#### 4. C IV VS. $H\beta$ AS A MASS DIAGNOSTIC

To test the hypothesis that  $R_{\text{BLR}}$  for C IV is typically half the value of that for  $H\beta$ , we compare the measured FWHM of C IV to that of  $H\beta$  (see Figure 4). If the velocities are virialized and  $R_{\text{BLR}}$  for C IV is half that of  $H\beta$ , we expect the FWHM of C IV to be a factor of  $\sqrt{2}$  larger than the FWHM of  $H\beta$ . FWHMs are estimated by an automated program as described in §3. There can be separate BLR and Narrow Line Region (NLR) contributions to  $H\beta$  (Marziani et al. 1996, Hamann et al. 1997), so each  $H\beta$  line is looked at individually. In 5 out of 74 cases, where there is obvious narrow  $H\beta$  emission with the same redshift and profile as [O III]  $\lambda 5007$ , this narrow emission is clipped off and the FWHM of  $H\beta$  is manually estimated. There appears to be no real correlation between the two FWHMs for individual objects, but averages of objects in selected ranges of C IV FWHM fall generally between a 1:1

correlation and the expected  $\sqrt{2}$ :1 correlation (see Figure 4). It should be noted that observations of  $H\beta$  and C IV for individual objects were not necessarily made simultaneously, which may contribute to the scatter in Figure 4. Five composite spectra, created from objects in selected ranges in SMBH mass (derived from C IV using Eqn. 4 and plotted as open boxes with error bars), do appear to be consistent with the expectation that  $\text{FWHM}(\text{C IV}) = \sqrt{2} \text{FWHM}(H\beta)$ . All spectra contributing to the composite spectra contain C IV, but only some contain  $H\beta$  (see Table 1). The narrow component of  $H\beta$  was not subtracted from any spectrum before the composite spectra were created. In the composites, the narrow  $H\beta$  contribution smoothly blends into the broad-line profile. Filled diamonds represent the averages of objects in selected ranges of C IV FWHM. These averages contain only the individual objects (plotted with + signs in the figure) that have data at both C IV and  $H\beta$ . Thus, while there is a large scatter among individual sources, the FWHMs of C IV and  $H\beta$  generally scale as expected in both the composite spectra and the averages of individual objects. Also note that any offsets in Fig. 4 affect only the absolute SMBH masses, with an uncertainty of up to a factor of two, but do not affect any trends with SMBH mass.

We also estimate the SMBH mass derived from C IV and the SMBH mass derived from  $H\beta$ . Masses are derived from  $H\beta$  using Eqns. 1 and 2. We compare the two masses for all objects in our sample that have observations of both lines (see Figure 5). Filled diamonds represent the averages of objects in selected ranges of SMBH mass (as derived from C IV). As in Fig. 4, these averages contain only the individual objects that have data at both C IV and  $H\beta$ . We find that there is approximately a 1:1 correlation between the mass obtained from C IV and that obtained from  $H\beta$ . There can be significant deviations from this for individual objects, but the relation holds well for averages of many objects. Hereafter, we will discuss only the masses obtained from C IV.

## 5. RESULTS

### 5.1. SMBH Mass vs. Redshift, Luminosity, and FWHM

Figure 6 shows the redshift distribution of the entire sample as a function of SMBH mass. The sample was designed to span the widest possible range of luminosity at each redshift, and the distribution of points in Fig. 6 closely follows the distribution in  $L$  vs.  $z$  (see Dietrich et al. 2002). There is no trend in SMBH mass with redshift. We expect SMBH mass to correlate with both continuum luminosity and FWHM because we derived our mass estimates from these quantities (Eqn. 4). Continuum luminosity is plotted as a function of SMBH mass in Figure 7, and shows the expected trend with little scatter. This relationship is much tighter than the relationship with the FWHM of C IV (see Figure 8), even though our SMBH mass estimates depend more sensitively on FWHM than luminosity. This may be due to the larger dynamic range in luminosity compared to FWHM (see Netzer 2003 for further discussion). In all three plots (Figs. 6-8), no trend is seen based on radio loud vs. radio quiet objects.

### 5.2. Line Properties versus SMBH Mass

The Baldwin Effect is an observed anti-correlation between continuum luminosity (and thus SMBH mass, since that is estimated based on luminosity) and the equivalent widths of emission lines such as C IV, Ly $\alpha$ , C III], and O VI (see Baldwin 1977; Croom et al. 2002; Dietrich et al. 2002; Espey et al. 1993; Osmer et al. 1994, Osmer & Shields 1999; Zheng & Malkan 1993). Interestingly, the Baldwin Effect is not seen in N V even though it seems to be present to some extent in N III]. Dietrich et al. (2002) discuss the Baldwin Effect of this same sample sorted by continuum luminosity. The Baldwin Effect is also evident in our spectra sorted by  $M_{\text{SMBH}}$ . Figure 9 plots rest-frame equivalent widths as a function of SMBH mass (see also Figs. 1 & 2). Al III curiously does not show the Baldwin Effect in these composite spectra and, if anything, its equivalent width actually increases with SMBH mass. This is contrary to its behavior in Dietrich et al. (2002) when sorted by continuum luminosity. The rest of the lines plotted in Fig. 9 show generally the same behavior as in Dietrich et al. (2002). Dietrich et al. (2002) find that the slope of the Baldwin Effect becomes steeper in most lines at higher luminosities. We observe a similar trend for steeper slopes at higher SMBH masses with the notable exception of N III], which slightly increases in REW at higher SMBH masses.

### 5.3. Metallicity versus SMBH Mass

Figure 10 shows the metallicities inferred by comparing emission line flux ratios for each composite spectrum to the theoretical results in Hamann et al. (2002). We obtain our metallicity estimates by comparing the emission line flux ratios to plots of metallicity vs. line ratio based on theoretical models (see Figure 5 in Hamann et al. 2002 and Figure 3 in Warner et al. 2002). We prefer to estimate the metallicities based on the calculations in Hamann et al. that use a segmented powerlaw for the photoionizing continuum shape. This continuum shape is a good approximation to the average observed continuum in quasars (Zheng et al. 1997; Laor et al. 1997). It also yields intermediate results for line ratios, such as N V/He II, that are sensitive to the continuum shape (see below).

The uncertainties in the metallicities shown in Figure 10 derive simply from the 1- $\sigma$  measurement uncertainties discussed in §3. They do not reflect the theoretical uncertainties in the technique we use to derive metallicities from the line ratios (see Hamann et al. 2002 for discussion). Also note that there is a larger statistical uncertainty in the lowest mass composite spectrum, because it is composed of only nine objects (the small number of spectra in this composite make it easier for one or two objects to dominate the composite).

Our best estimate of the overall metallicity from each spectrum (labeled as Average in Fig. 10) is obtained by averaging the results of N III]/C III], N III]/O III], N V/C IV, and N V/O VI. We select these ratios because we believe they are the most accurately measured ratios and the most reliable from a theoretical viewpoint (Hamann et al. 2002).

We believe the ratios involving N IV] are less reliable for several reasons. First, the N IV] flux is difficult to measure because this line is weak and in the wing of the much stronger C IV line profile. Second, ratios such as N IV]/C IV, which compare a permitted and intercombi-

nation line, are potentially more sensitive to uncertainties in the line optical depths and radiative transfer. Third, perhaps as a consequence of the greater uncertainties in N IV], there is more object-to-object scatter in the results derived from N IV] compared to N III] (Hamann et al. 2002). We also exclude N V/He II from our estimate of the average metallicity because i) this ratio compares a collisionally excited line (N V) to a recombination line (He II), and ii) it can yield (for this continuum shape) very high metallicities that are obtained by extrapolations beyond the theoretical results calculated by Hamann et al. (2002).

All of the line ratios involving N III] and N V show N/O and N/C ratios that are solar or greater. This implies a metallicity of  $\gtrsim 1 Z_{\odot}$  if N is mostly secondary.

### 5.4. Do N III] and N V Disagree?

All four ratios involving N V show a strong trend in metallicity with SMBH mass. The slope of this trend is not linear and seems to increase as mass increases. The ratios involving N III], however, show no apparent correlation between metallicity and SMBH mass. We believe that this apparent discrepancy between the two ratios may be due to the large FWHMs and small REWs of the emission lines in the composite spectra representing higher SMBH masses.

The spectra representing higher SMBH masses have broader lines because the mass derivation depends on the line FWHM (Eqn. 4). This may lead to systematic overestimating of the continuum if the wings of the lines blend together and never quite reach the continuum level. In particular, notice the interval around 1460 Å (see Figs. 1 and 2) that we used to constrain our continuum fits (see §3). In the higher mass spectra, C IV and Si IV + O IV] seem to blend together, never quite reaching the true continuum, and instead forming a “U” shape. This effect of overestimating the continuum could lead to underestimates of N III] and N IV] in the higher mass spectra and thus negate or weaken any real trend between SMBH mass and the flux ratios involving these lines. For example, we find that a drop in the continuum level of only 5% will more than double the measured flux in N III] and N IV], but increase the flux in stronger lines by only  $\sim 15\%$  to 30%.

In order to more thoroughly examine the effects of FWHM on the measured line fluxes, we sort the quasar spectra by the FWHM of C IV and create composite spectra for different ranges in FWHM. We then fit the continuum and measure the emission line fluxes as described in §3. The resulting line ratios are plotted in Figure 11. We find that the flux ratio of C III]/C IV remains roughly constant at different line widths, but N III]/N V declines as the lines get broader. Because of this, we again see a discrepancy in metallicity trends between ratios involving N III] and those involving N V. The ratios involving N V indicate increasing metallicity with increasing line width. This is expected because objects with broader emission lines should have higher black hole masses and thus higher metallicities (§1). The N III] ratios, however, show a “U”-like behavior in Figure 11, with the narrowest lines having the highest metallicity. The composite spectrum with the narrowest lines is also the only one in which the metal-

licities derived from N III] ratios agree with those derived from N V ratios.

There are two possible explanations for the discrepancy between the line ratios. The first possibility is that N V is somehow enhanced in quasars with broader emission lines (and/or larger  $L$  and  $M_{\text{SMBH}}$ ) by a process that we do not understand. The second possibility is that we are systematically overestimating the continuum and thus underestimating the flux of N III] in spectra with broader lines. There is evidence supporting the latter hypothesis in that N III]/N V and C III]/C IV behave similarly in our overall quasar sample. In particular, when N III]/N V is larger/smaller than average, C III]/C IV is also larger/smaller by roughly the same factor. The inter-combination lines scale roughly together compared to the permitted lines of the same element. The somewhat different behaviors of N III]/N V and C III]/C IV in Figure 11 (sorted by FWHM) therefore suggest that we are underestimating the weak N III] line in the broader line sources. The U-like shape of the N III]/O III] and N III]/C III] points in this figure could then be caused by an increasing underestimate of N III] as the FWHM increases from  $\sim 2000 \text{ km s}^{-1}$  to  $\sim 5000 \text{ km s}^{-1}$ , offset by the increasing N/O and N/C abundance ratios for FWHM  $\gtrsim 5000 \text{ km s}^{-1}$ . Thus, we believe this is the more likely scenario. This scenario may also explain the fact that the metallicities derived from all ratios agree for objects with narrow emission lines (see also Warner et al. 2002; Baldwin et al. 2003), in which the continuum is unlikely to be systematically overestimated.

## 6. DISCUSSION

Our main result from §5 is that the data are consistent with a trend between BLR metallicity and SMBH mass. The hypothesis motivating this work (§1) was that there should be a trend between metallicity and SMBH mass with roughly the same slope as the mass-metallicity relation in elliptical galaxies, if the BLR gas was enriched by stars in the AGN’s host galaxy. We use a plot of  $\text{Mg}_2$  index vs. velocity dispersion,  $\sigma$ , in Bender et al. (1993) to estimate the slope of the galactic mass-metallicity relation.  $\text{Mg}_2$  index is a line strength parameter used to derive metallicities. Bender et al. (1993) derive  $\log(\text{Mg}_2) \propto 0.41 \log(Z/Z_{\odot})$  and  $\log(\text{Mg}_2) \propto 0.20 \log(\sigma)$ . Using these proportionalities, along with  $M \propto \sigma^2$ , we obtain an estimate of the slope of the mass-metallicity relation in log space,  $\Delta Z/\Delta M \sim 0.24$ . We obtain a similar estimate ( $\Delta Z/\Delta M \sim 0.34$ ) using a plot of [O/H] vs. absolute blue magnitude in Zaritsky et al. (1994) combined with a plot of  $\log(L_B)$  vs.  $\log(M)$  in van Albada et al. (1995). We also derive  $\log(Z) \propto 0.38 \pm 0.07 \log(M_{\text{SMBH}})$  from the  $[Z/H] \propto 0.76 \pm 0.13 \log(\sigma)$  relation given in Trager et al. (2000). We employ a  $\chi^2$  minimization routine to obtain linear fits to the plots of metallicity vs. SMBH mass shown in Figure 10. These fits yield a slope of  $\Delta Z/\Delta M \sim 0.2 - 0.3$  for all ratios involving N V. This is consistent with the slope of the mass-metallicity relation in elliptical galaxies as expected. The slope for the average metallicity vs. SMBH mass is  $\sim 0.2$ , slightly lower than the slopes for the N V ratios. The slope for ratios involving N III] is  $\sim 0$ , but the slope from only the three highest mass spectra for these ratios is  $\sim 0.1 - 0.2$ . This may be a lower

bound on the slope of metallicity vs. SMBH mass because in the highest mass spectra, the increasing N/O and N/C abundance ratios are starting to dominate the underestimation of N III] caused by the systematic overestimation of the continuum in spectra with broad lines.

It should be noted that the quasar-BLR metallicities are several times higher than the galactic values derived in the studies listed above. This apparent discrepancy can be understood in the context of normal galaxy evolution. Quasar BLRs sample an earlier evolutionary stage and frequently a different physical location in galaxies compared to the H II regions or average spectra of stars in present day galaxies (Hamann & Ferland 1999). However, the similar slope of the mass-metallicity relationship in both quasars and galaxies supports the premise that the gas in the BLR was processed/enriched by the surrounding stellar population.

The evidence presented here for a mass-metallicity relationship among quasars does not prove that SMBH mass is the fundamental parameter affecting BLR metallicity. However, in these composite spectra, sorted by SMBH mass, the slope of the trend between *luminosity* and metallicity is at least as steep as (and possibly marginally steeper than) the slope is for composite spectra sorted by luminosity (see Dietrich et al. 2002; Dietrich et al. 2003, in prep). Also, composite spectra created from different ranges in Eddington ratio,  $L_{\text{bol}}/L_{\text{edd}}$ , show a slight trend with luminosity, but no trend with either SMBH mass or metallicity (see Warner et al. 2003, in prep). These results suggest that SMBH mass could be the fundamental parameter. Further support for mass as the fundamental parameter comes from the similarity of the mass-metallicity relationship among quasars to the corresponding relationship among galaxies. These ideas are also consistent with the growing evidence (e.g. Shields et al. 2002) for a close relationship between quasars and their host galaxies. In particular, the relationship between SMBH mass and host galaxy mass (see refs. in §1) indicates that i) SMBHs are a natural byproduct of galaxy formation, and ii) essentially all massive galaxies were at one time “active.” Quasars at high redshifts are signposts of the last stages in the formation of these massive SMBHs in the cores of young galactic spheroids. The high metallicities near these objects reported here and elsewhere (Constantin et al. 2001; Dietrich et al. 1999, 2003; Hamann 1997; Hamann & Ferland 1999; Hamann et al. 2002; Osmer et al. 1994; Petitjean et al. 1994; Warner et al. 2002) imply that the gas has *already* (at the quasar epoch) been substantially processed/enriched by multiple generations of massive stars. This rapid evolution at high redshifts, though, is well within the parameters derived in some recent simulations, which show that the densest protogalactic condensations can form stars and reach solar or higher metallicities at  $z \gtrsim 6$  (Gnedin & Ostriker 1997; Haiman & Loeb 2001).

## 7. SUMMARY & CONCLUSIONS

We have investigated a large sample of 578 AGNs for a trend between metallicity and SMBH mass. The sample covers a redshift range from  $0 \lesssim z \lesssim 5$ , six orders of magnitude in luminosity, and five orders of magnitude in SMBH mass. We estimate SMBH masses using the virial

theorem and formulae given in Kaspi et al. (2000). To improve the signal-to-noise ratio and average over object-to-object variations, we produce composite spectra representing each decade in SMBH mass. Composite spectra allow us to better measure weak emission lines and minimize the influence of irregularities in any individual quasar. After a powerlaw continuum fit, multi-component Gaussian profiles are fit to emission lines to measure their fluxes. Metallicities are then estimated by comparing emission line ratios involving nitrogen to theoretical predictions in Hamann et al. (2002). Our main results are as follows.

1) We estimate SMBH masses based on both C IV and  $H\beta$  and find approximately a 1:1 correlation for averages of many objects (Fig. 5). We conclude that it is valid to use C IV instead of  $H\beta$  to estimate average black hole masses in samples of AGNs.

2) There is no trend between SMBH mass and redshift, but as expected, SMBH mass shows a positive correlation with both luminosity and the FWHM of C IV.

3) We observe the usual Baldwin Effect in composite spectra representing different ranges in SMBH mass. In agreement with other studies (see Dietrich et al. 2002), N V does not show the Baldwin Effect even though it seems to be present to some extent in N III]. However, Al III curiously does not exhibit the Baldwin Effect either, and if anything, its REW actually increases with increasing SMBH mass.

4) We find a trend in metallicity with SMBH mass for emission line ratios involving N V, but not for those involving N III] or N IV]. This is consistent with the findings of Dietrich et al. (2002). They find a lack of a Baldwin Effect for N V, which in the present study leads to emission line ratios involving N V increasing with increasing

luminosity. However, Dietrich et al. (2003a, 2003b) find that metallicities derived from ratios involving both N III] and N V yield results of solar or greater, for samples of 70 high redshift ( $3.9 \lesssim z \lesssim 5.0$ ) quasars.

5) We conclude that the data are consistent with a trend between SMBH mass and metallicity and some of the data (N V ratios) indicate that there is a very strong trend. N III] seems to indicate no trend; however, upon further examination, we believe that the uncertainties in N III] and N IV] are too large to confirm or test any trend. We note that the correlation between SMBH mass and FWHM may lead to systematic overestimates of the continuum and thus underestimates of N III] and N IV] in the higher mass spectra.

6) We estimate the slope of the galactic mass-metallicity relationship in log space to be  $\Delta Z/\Delta M \sim 0.2 - 0.3$  (see §6). This slope is consistent with linear fits to the plots of metallicity vs. SMBH mass in Fig. 10 that are derived from ratios involving N V, as well as the plot of “average” metallicity vs. SMBH mass. The similarity in the slope of the mass-metallicity relationship in both quasars and galaxies supports the premise that the gas in the BLR was processed/enriched by the surrounding stellar environment and contributes to the growing evidence for a close relationship between quasars and their host galaxies.

*Acknowledgements:* We are very grateful to Marianne Vestergaard for providing the UV Fe emission template for this study and to Fred Chaffee, Anca Constantin, Craig Foltz, Vesa Junkkarinen, and Joe Shields for their direct participation in reducing or acquiring some of the ground-based spectra. We acknowledge financial support from the NSF via grant AST99-84040 and NASA via grant NAG5-3234.

## APPENDIX

We fit C IV  $\lambda 1549$  with three Gaussian profiles. Three Gaussians are necessary to obtain a good fit because the emission lines are not Gaussian by nature and contain broad wings. We ignore the doublet splitting in C IV because it is small compared to the observed line widths. N IV]  $\lambda 1486$ , where it is measureable, is fit with a C IV profile. That is, we fit it with three Gaussian profiles that have their FWHMs tied to the values fit to C IV and their relative fluxes and relative wavelength shifts are tied to the same ratios as in the fit to C IV. For the two highest mass composite spectra, we fit only an upper-bound to N IV] because it is too blended with the wing of C IV to measure. He II  $\lambda 1640$  is fit with two Gaussian profiles, one broad and one narrow and O III]  $\lambda 1665$  is fit with a C IV profile. The weak and badly blended doublet Si II  $\lambda\lambda 1527, 1533$  is fit with one Gaussian profile for each component.

Ly $\alpha$   $\lambda 1216$ , like C IV, is fit with three Gaussian profiles, but only the red side of the line is used for  $\chi^2$  minimization because of contamination by the Ly $\alpha$  forest on the blue side. Each component of the N V  $\lambda 1240$  doublet is fit with a C IV profile because N V is strongly blended with the wing of Ly $\alpha$ . This connection between C IV and N V can be justified because they are both high ionization lines with similar excitation properties (Ferland et al. 1998). The relative fluxes of the two components of the N V doublet are set to the ratio of the statistical weight,  $g$ , times the  $A$  value for each transition (approximately 2:1 in this case), because this yields a better fit than using a 1:1 ratio. We use atomic data obtained from the National Institute of Standards and Technology (<http://aeldata.phy.nist.gov/PhysRefData/contents-atomic.html>) to calculate  $g$  times the  $A$  value for each transition. The weak and blended multiplet Si II  $\lambda\lambda 1260, 1264, 1265$  is fit with one Gaussian profile for each component.

We fit O I  $\lambda 1303$  with a single Gaussian profile and C II  $\lambda 1335$  with two Gaussians, one for each component of the doublet. The fluxes of the two C II components are tied to a 1:1 ratio because this yields a better fit than a 2:1 ratio. The FWHMs and relative wavelengths are also tied together.

We fit the doublet Si IV  $\lambda\lambda 1393, 1403$  with one Gaussian profile for each of the two components. The fluxes of these components are tied to a 1:1 ratio because this yields a better fit than a 2:1 ratio. O IV]  $\lambda 1403$ , a blended multiplet of five lines, is fit with one Gaussian profile for each of its five components. The flux ratios of the components in this case are tied to the ratio of  $g$  times the  $A$  value for each transition using atomic data obtained from Nussbaumer & Storey (1982). Because Si IV and O IV] are badly blended, we tie the FWHMs and relative wavelengths together for all seven components of the Si IV - O IV] blend. We list the sum of the blend in Table 2.

We fit the N III]  $\lambda$ 1750 multiplet with five C IV profiles, one for each component of the multiplet. We use C IV profiles to constrain the fit because N III] is a weak intercombination line. The relative fluxes of the five components are tied to the ratio of  $g$  times the  $A$  value for each transition because this yields the best fit. The FWHMs and relative wavelengths are all tied together.

We use two Gaussian profiles to fit C III]  $\lambda$ 1909 because two Gaussians provide a fit that is just as good as the fit obtained by using three Gaussians. The Al III  $\lambda\lambda$ 1855, 1863 doublet is fit with one Gaussian profile for each component. The flux ratio is tied to the ratio of  $g$  times the  $A$  value for each transition and the FWHMs and relative wavelengths of both components are tied together. Si III]  $\lambda$ 1892 is fit with one Gaussian profile and has its FWHM and relative wavelength tied to Al III because it is badly blended with C III].

We fit a local continuum around O VI  $\lambda$ 1035, which was constrained by the flux in wavelength intervals centered at 960 Å and 1100 Å. We then fit each component of the O VI  $\lambda$ 1035 doublet with two Gaussian profiles. The fluxes are tied to a 3:2 ratio, compromising between 1:1 and 2:1, because this yields the best fit. Where they are measureable, C III  $\lambda$ 977 and N III  $\lambda$ 990 are fit with one Gaussian profile each, and their FWHMs and relative wavelengths are tied together. When calculating fluxes from measured REWs, we scale O VI as if it were sitting on top of a segmented powerlaw continuum, defined by our previous continuum fit redward of 1250 Å and by a powerlaw with index  $\alpha = -1.76$  (Telfer et al. 2002) blueward of 1250 Å.

Each of the five spectra is fit in this fashion, with the following exceptions for the broadest ( $M \sim 10^{10} M_{\odot}$ ) spectrum, which has many extremely blended lines. In this spectrum, we tie the relative wavelengths of the three Gaussian profiles used to fit C IV and Ly $\alpha$  and the two Gaussian profiles used to fit C III] to the corresponding ratios from our fit to the  $M \sim 10^9 M_{\odot}$  sample. We do not attempt to fit N IV] or Si II  $\lambda\lambda$ 1527, 1533, as they are undetectable due to the broad wing of C IV. It should also be noted that in our fit to this spectrum, the broader Gaussian profile of our fit to He II is blueshifted by 15 Å.

## REFERENCES

- Baldwin, J. A. 1977, ApJ, 214, 679  
 Baldwin, J. A., Hamann, F., Korista, K. T., Ferland, G. J., Dietrich, M., & Warner, C. 2003, ApJ, 583, 649  
 Bender, R., Burnstein, D., & Faber, S. M. 1993, ApJ, 411, 153  
 Bettoni, D., Falomo, R., Fasano, G., & Govoni, F. 2003, A&A, 399, 869  
 Brotherton, M. S. et al. 2001, ApJ, 546, 775  
 Carroll, S. M., Press, W. H., & Turner, E. L. 1992, ARA&A, 30, 499  
 Constantin, A., Shields, J. C., Hamann, F., Foltz, C., & Chaffee, F. 2001, ApJ, 565, 50  
 Corbett, E. A. et al. 2003, astro-ph/0304541  
 Croom, S. M. et al. 2002, MNRAS, 337, 275  
 Dietrich, M. et al. 1999, A&A, 352, L1  
 Dietrich, M., Hamann, F. et al. 2002, ApJ, 581, 912  
 Dietrich, M. et al. 2003a, A&A, 398, 891  
 Dietrich, M., Hamann, F. et al. 2003b, ApJ, 589, in press  
 Erwin, P., Graham, A. W., & Caon, N. 2002, astro-ph/0212335  
 Espey, B. R., Lanzetta, K. M., & Turnshek, D. A. 1993, BAAS, 25, 1448  
 Faber, S. M. 1973, ApJ, 179, 731  
 Ferland, G. J. et al. 1996, ApJ, 461, 683  
 Ferland, G. J. et al. 1998, PASP, 110, 761  
 Ferrarese, L. & Merritt, D. 2000, ApJ, 539, L9  
 Ferrarese, L. et al. 2001, ApJ, 555, L79  
 Ferrarese, L. & Merritt, D. 2002, astro-ph/0206222  
 Gebhardt, K. et al. 2000a, ApJ, 539, L13  
 Gebhardt, K. et al. 2000b, ApJ, 543, L5  
 Gnedin, N. Y. & Ostriker, J. P. 1997, ApJ, 486, 581  
 Graham, A. W., Erwin, P., Caon, N., & Trujillo, I. 2001, ApJ, 563, L11  
 Haiman, Z. & Loeb, A. 2001, ApJ, 552, 449  
 Hamann, F. & Ferland, G. 1992, ApJ, 391, L53  
 Hamann, F. & Ferland, G. 1993, ApJ, 418, 11  
 Hamann, F. 1997, ApJS, 109, 279  
 Hamann, F. et al. 1997, ApJ, 488, 155  
 Hamann, F., Shields, J. C., Burbridge, E. M., Junkkarinen, V., & Crenshaw, D. M. 1998, ApJ, 496, 761  
 Hamann, F. & Ferland, G. 1999, ARA&A, 37, 487  
 Hamann, F., Korista, K. T., Ferland, G. J., Warner, C., & Baldwin, J. 2002, ApJ, 564, 592  
 Henry, R. B. C., Edmunds, M. G., & Köppen, J. 2000, ApJ, 541, 660  
 Jablonka, P., Martin, P., & Arimoto, N. 1996, AJ, 112, 1415  
 Kaspi, S., Smith, P. S., Netzer, H., Maoz, D., Jannuzi, B. T., & Giveon, U. 2000, ApJ, 533, 631  
 Korista, K.T. et al. 1995, ApJS, 97, 285  
 Kriss, G. 1994, in ASP Conf. Ser. 61, Astronomical Data Analysis Software and Systems III, eds. D. R. Crabtree, R. J. Hanisch, & J. Barnes (San Francisco: ASP), 437  
 Laor, A. et al. 1994, ApJ, 420, 110  
 Laor, A., Jannuzi, B. T., Green, R. F., & Boroson, T. A. 1997, ApJ, 489, 656  
 Laor, A. 1998, ApJ, 505, L83  
 Magorrian, J. et al. 1998, AJ, 115, 2285  
 Marziani, P., Sulentic, J. W., Dultzin-Hacyan, D., Calvani, M., & Moles, M. 1996, ApJS, 104, 37  
 McLure, R. J. & Dunlop, J. S. 2001, MNRAS, 327, 199  
 McLure, R. J. & Dunlop, J. S. 2002, MNRAS, 331, 795  
 McLure, R. J. & Jarvis, M. J. 2002, MNRAS, 337, 109  
 Merritt, D. & Ferrarese, L. 2001, ApJ, 547, 140  
 Netzer, H. 2003, ApJ, 583, L5  
 Nussbaumer, H. & Storey, P. J. 1982, A&A, 115, 205  
 Osmer, P., Porter, A. C., & Green, R. F. 1994, ApJ, 436, 678  
 Osmer, P. & Shields, J. C. 1999, La Serena Conference on 'Quasars and Cosmology', eds. G. Ferland & J. Baldwin  
 Peterson, B. M. 1993, PASP, 105, 247  
 Peterson, B. M. 1997, An Introduction to Active Galactic Nuclei (Cambridge: Cambridge University Press)  
 Peterson, B. M. & Wandel, A. 1999, ApJ, 521, L95  
 Peterson, B. M. & Wandel, A. 2000, ApJ, 540, L13  
 Petitjean, P., Rauch, M., & Carswell, R. F. 1994, A&A, 291, 29  
 Pettini, M., Ellison, S. L., Bergeron, J., & Petitjean, P. 2002, A&A, 391, 21  
 Pilyugin, L. S., Mollá, M., Ferrini, F., & Vílchez, J. M. 2002, A&A, 383, 14  
 Shields, G. A. 1976, ApJ, 204, 330  
 Shields, G. A. et al. 2002, astro-ph/0210050  
 Stirpe, G. M. et al. 1994, ApJ, 425, 609  
 Telfer, R. C., Zheng, W., Kriss, G. A., & Davidsen, A. F. 2002, ApJ, 565, 773  
 Trager, S. C., Faber, S. M., Worthey, G., & Gonzalez, J. J. 2000, AJ, 120, 165  
 Tremaine, S. et al. 2002, ApJ, 574, 740  
 Tinsley, B. 1980, Fundam. Cosmic Physics, 5, 287  
 van Albada, T. S., Bertin, G., & Stiavelli, M. 1995, MNRAS, 276, 1255  
 van Zee, L., Salzer, J. J., & Haynes, M. P. 1998, ApJ, 497, L1  
 Vanden Berk, D. E. et al. 2001, AJ, 122, 549  
 Verner, E. M. et al. 1999, ApJS, 120, 101  
 Véron-Cetty, M.-P. & Véron, P. 2001, "A Catalogue of Quasars and Active Nuclei", 10th edition  
 Vestergaard, M. & Wilkes, B. J. 2001, ApJS, 134, 1  
 Vestergaard, M. 2002, ApJ, 571, 733  
 Wandel, A. 1999, ApJ, 519, L39  
 Wandel, A., Peterson, B. M., & Malkan, M. A. 1999, ApJ, 526, 579  
 Warner, C., Hamann, F., Shields, J. C., Constantin, A., Foltz, C., & Chaffee, F. 2002, ApJ, 567, 68  
 Wills, B. J., Brotherton, M. S., Fang, D., Steidel, C. C., & Sargent, W. L. W. 1993, ApJ, 415, 563  
 Zaritsky, D., Kennicutt, R. C., & Huchra, J. P. 1994, ApJ, 440, 606  
 Zheng, W. & Malkan, M. A. 1993, ApJ, 415, 517  
 Zheng, W., Kriss, G. A., Telfer, R. C., Grimes, J. P., & Davidsen, A. F. 1997, ApJ, 475, 469

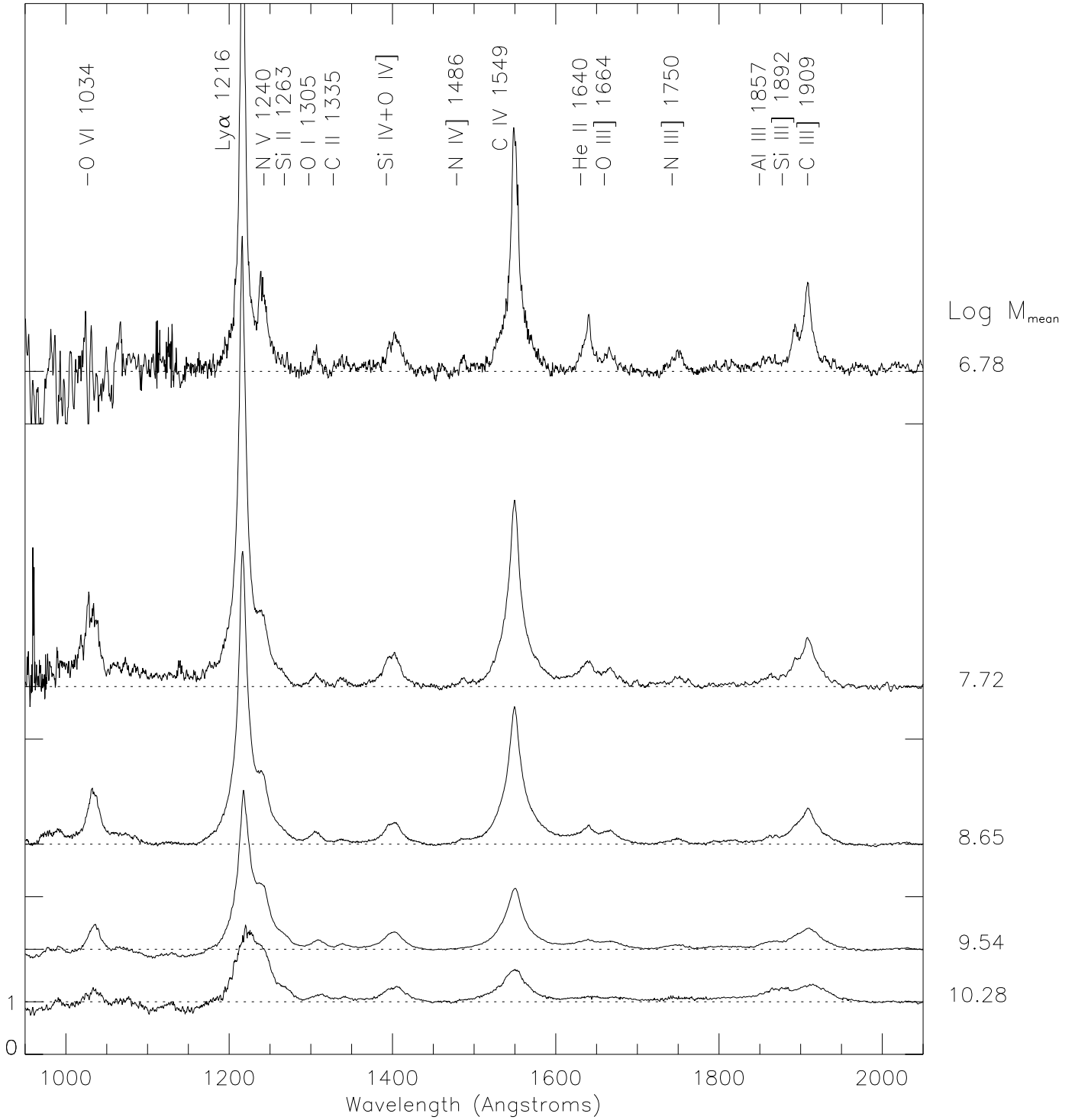


FIG. 1.— Normalized composite spectra are shown for all five SMBH mass bins. The spectra were normalized by a power law continuum fit. The horizontal dashed lines indicate the continuum level for the individual normalized composite spectra, which were vertically shifted for better display. The normalized continuum strength is shown for the spectrum at the bottom of the figure. This same vertical scale applies to all other spectra, although the tick marks for '0' and '1' are not labelled. The mean SMBH mass of each spectra is listed to the right. The Baldwin Effect is clearly seen in these spectra.

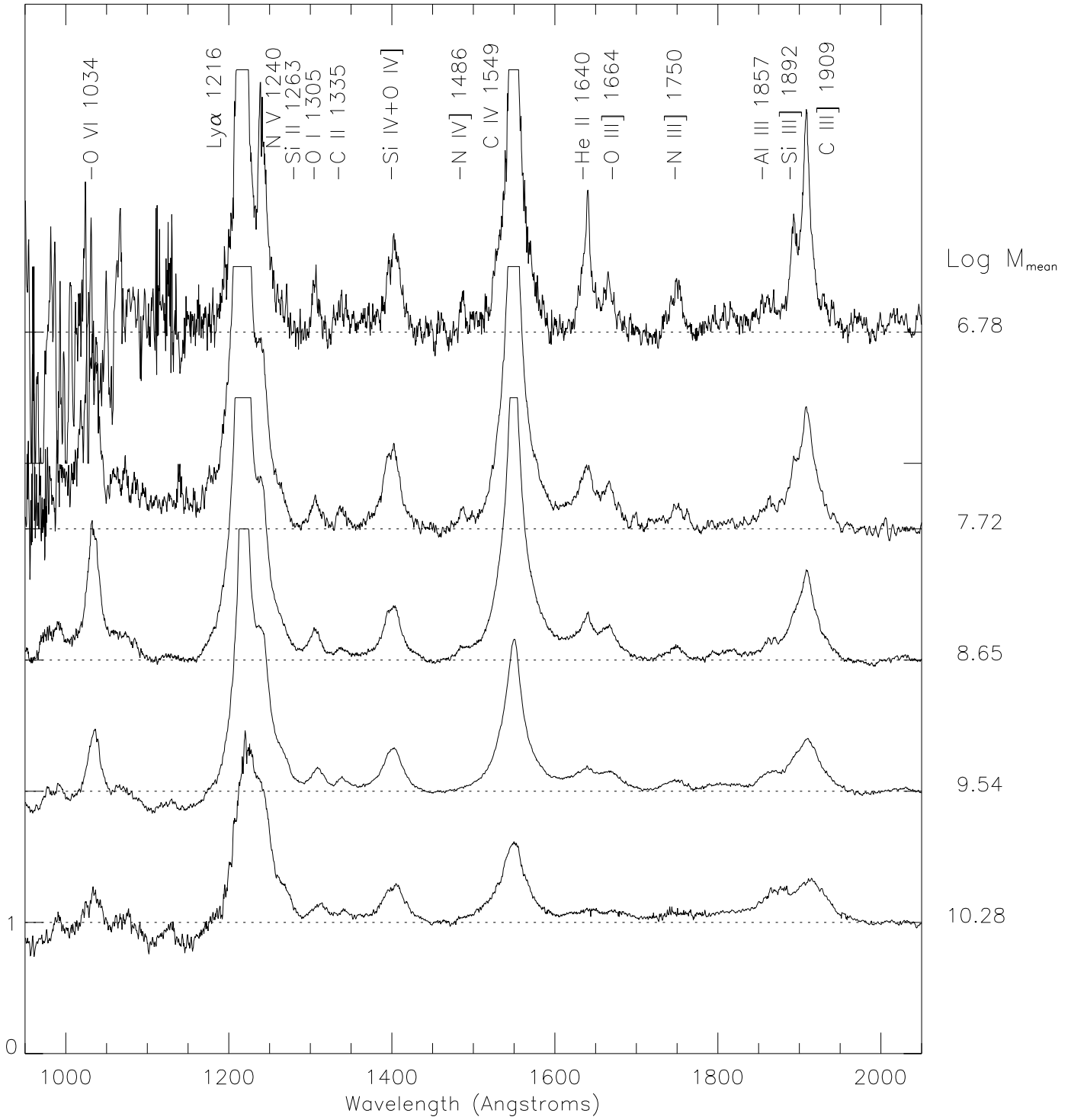


FIG. 2.— Same as Fig. 1, but with an expanded vertical scale to display the dependence of the relative strength of weaker emission lines as a function of SMBH mass. Strong emission lines with flat tops are truncated for easier display.

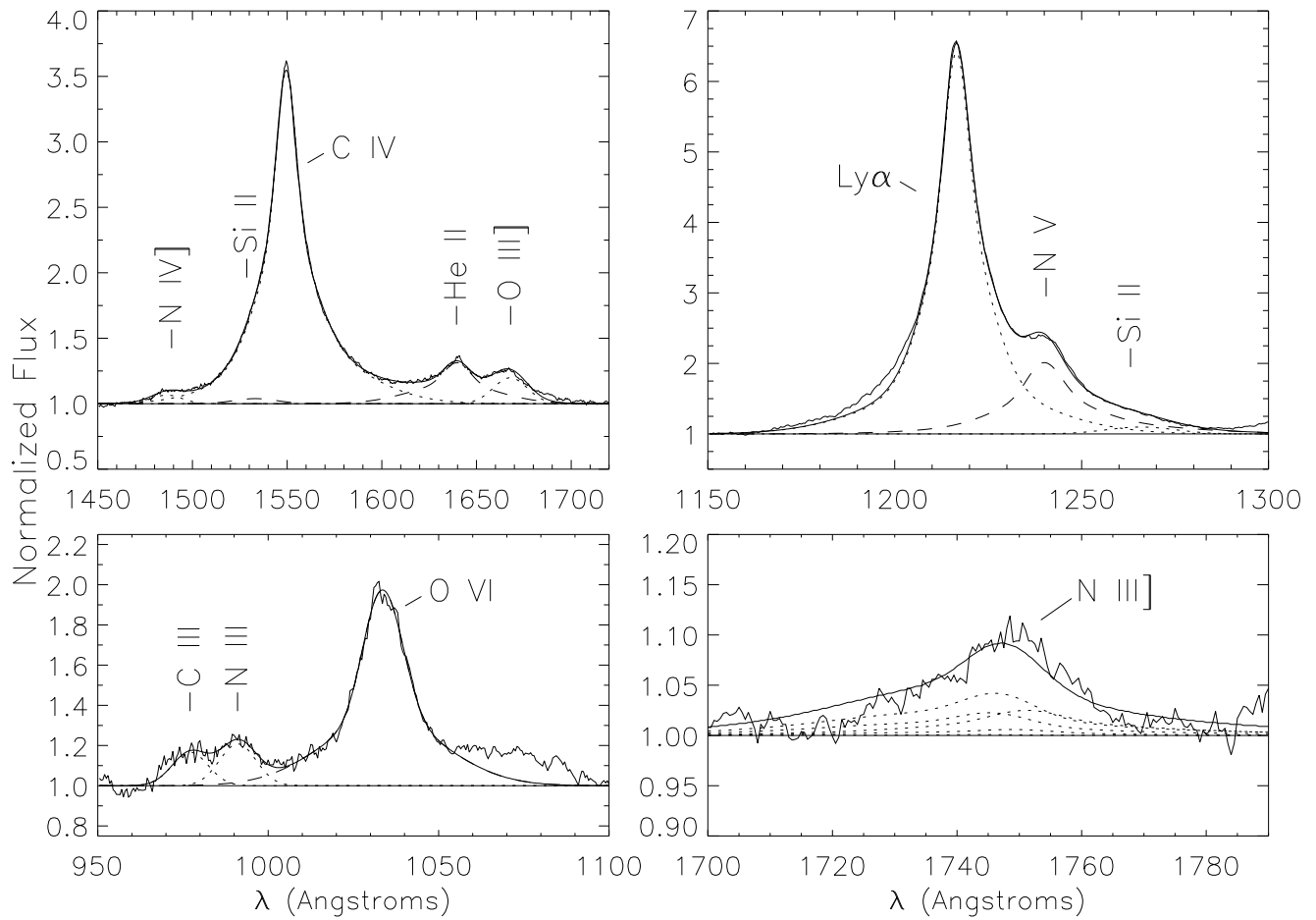


FIG. 3.— Multi-component Gaussian fits (smooth solid curves) to observed emission lines (jagged solid curves) for a composite spectrum of  $M \sim 10^8 M_{\odot}$ . The continuum is normalized by a power law continuum fit. The continuum (at unity) and composite line fits are plotted. The individual Gaussian components of the fits are shown for the fit to N III] as dotted lines. In the other panels, the dashed and dotted lines represent the sum contribution of each labelled emission line. There is an unidentified bump at  $\sim 1070 \text{ \AA}$  that is not attributed to O VI (see Hamann et al. 1998).

TABLE 1  
COMPOSITE PARAMETERS

Log $M_{\text{SMBH}}$ [ $M_{\odot}$ ]	$\alpha$	# Objects at C IV	FWHM(C IV) [ $\text{km s}^{-1}$ ]	# Objects at $H\beta$	FWHM( $H\beta$ ) [ $\text{km s}^{-1}$ ]	Log $\lambda L_{\lambda}(1450\text{\AA})$ [ $\text{ergs s}^{-1}$ ]	Log $M_{\text{mean}}$ [ $M_{\odot}$ ]
6 – 7	-0.98	7	2100	4	1400	44.0	6.78
7 – 8	-0.90	61	3300	31	2250	45.0	7.27
8 – 9	-0.71	198	3900	35	3000	46.2	8.65
9 – 10	-0.59	261	4900	6	3650	46.9	9.54
> 10	-0.57	34	6500	1	4500	47.5	10.28

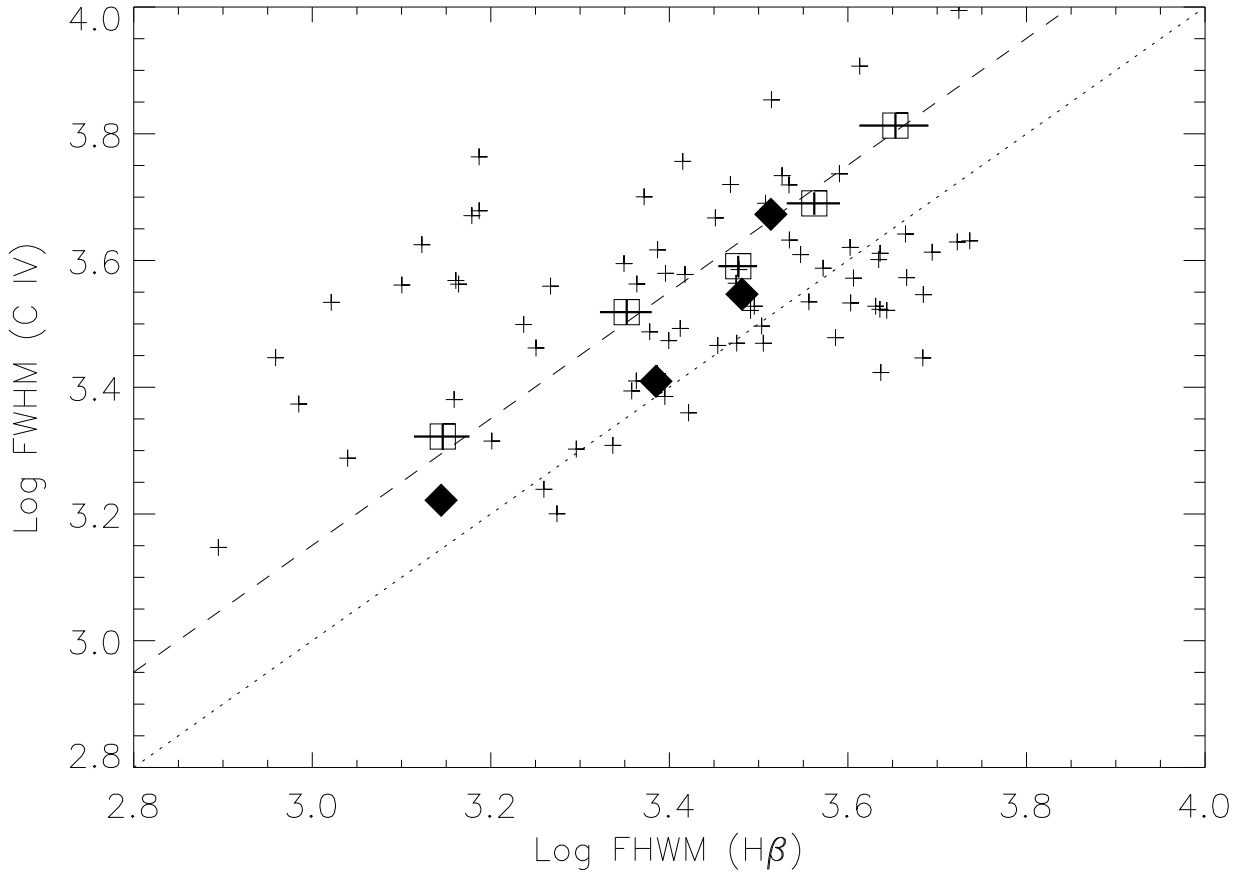


FIG. 4.— Comparison of the measured FWHM of C IV to that of  $H\beta$  for all objects in our sample with observations of both lines. In five cases, obvious narrow  $H\beta$  emission was subtracted prior to measuring its FWHM. The open boxes represent five composite spectra created from objects in selected ranges of SMBH mass. The error bars drawn on the boxes represent the  $\pm 1\sigma$  ranges for the FWHMs of C IV and  $H\beta$  for these composite spectra. The filled diamonds represent averages of objects in selected ranges of C IV FWHM ( $< 2000$  km/s, 2000–3000 km/s, 3000–4000 km/s, and 4000–6000 km/s). The dotted line is a 1:1 ratio and the dashed line is the expected ratio of  $\text{FWHM}(\text{C IV}) = \sqrt{2} \text{FWHM}(\text{H}\beta)$ .

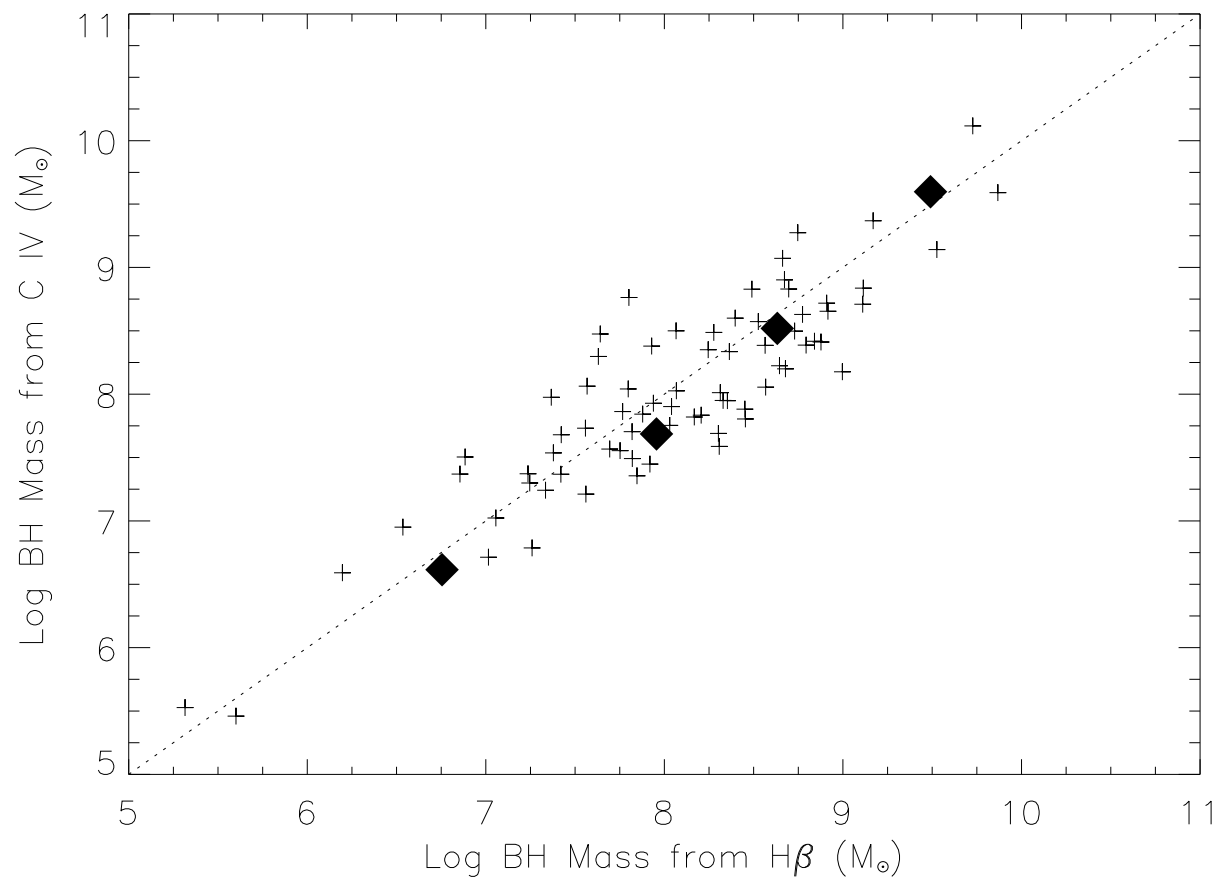


FIG. 5.— Comparison of the SMBH mass derived from C IV to that derived from  $H\beta$  for all objects in our sample with observations of both lines. The filled diamonds represent averages of objects in selected SMBH mass ranges. The dotted line is a 1:1 ratio (the RMS scatter about the 1:1 relationship is 0.39 for the individual objects and 0.17 for the averages). For composite spectra of many objects, both methods yield approximately the same mass.

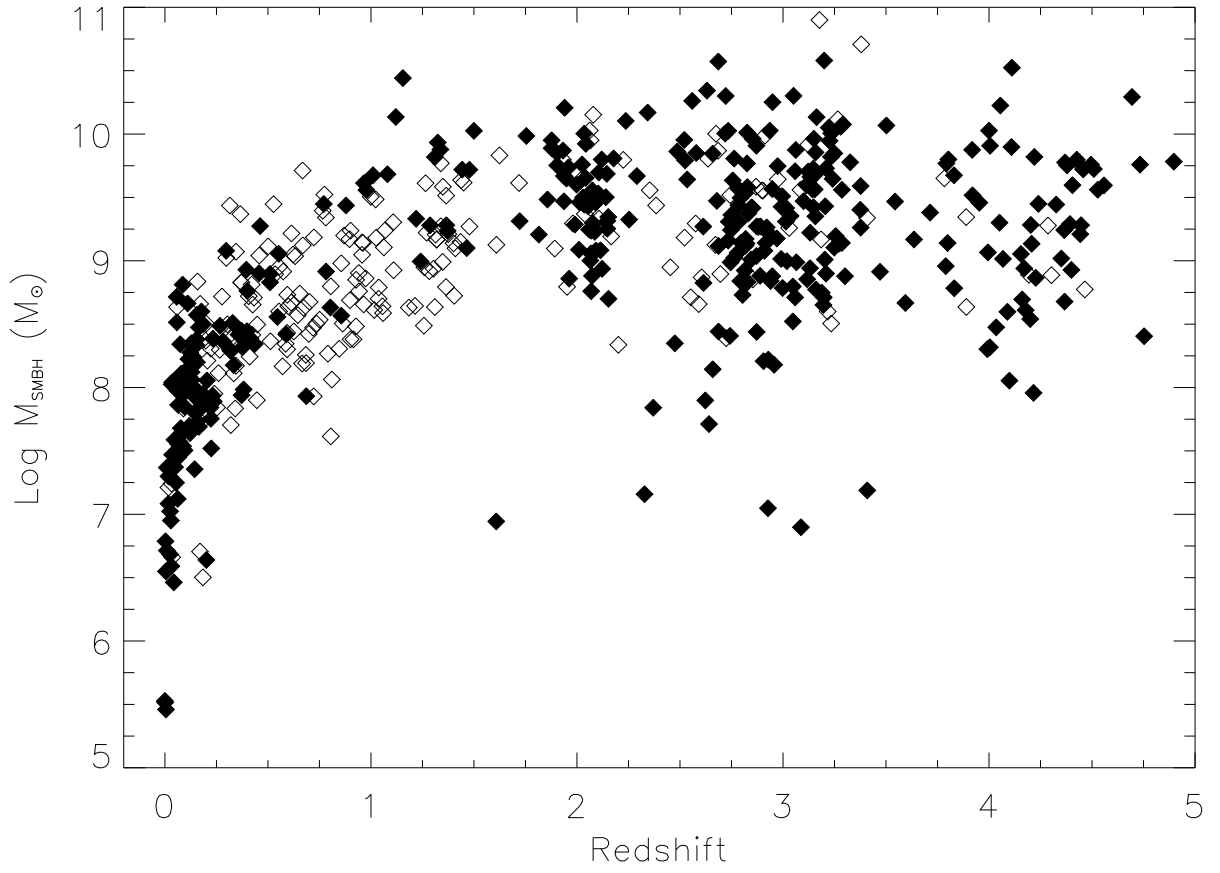


FIG. 6.— Redshift distribution of the AGN sample as a function of SMBH mass. The filled diamonds represent radio-quiet quasars and the open diamonds represent radio-loud quasars. There is clearly no trend in SMBH mass with redshift (for  $z \gtrsim 0.3$ ).

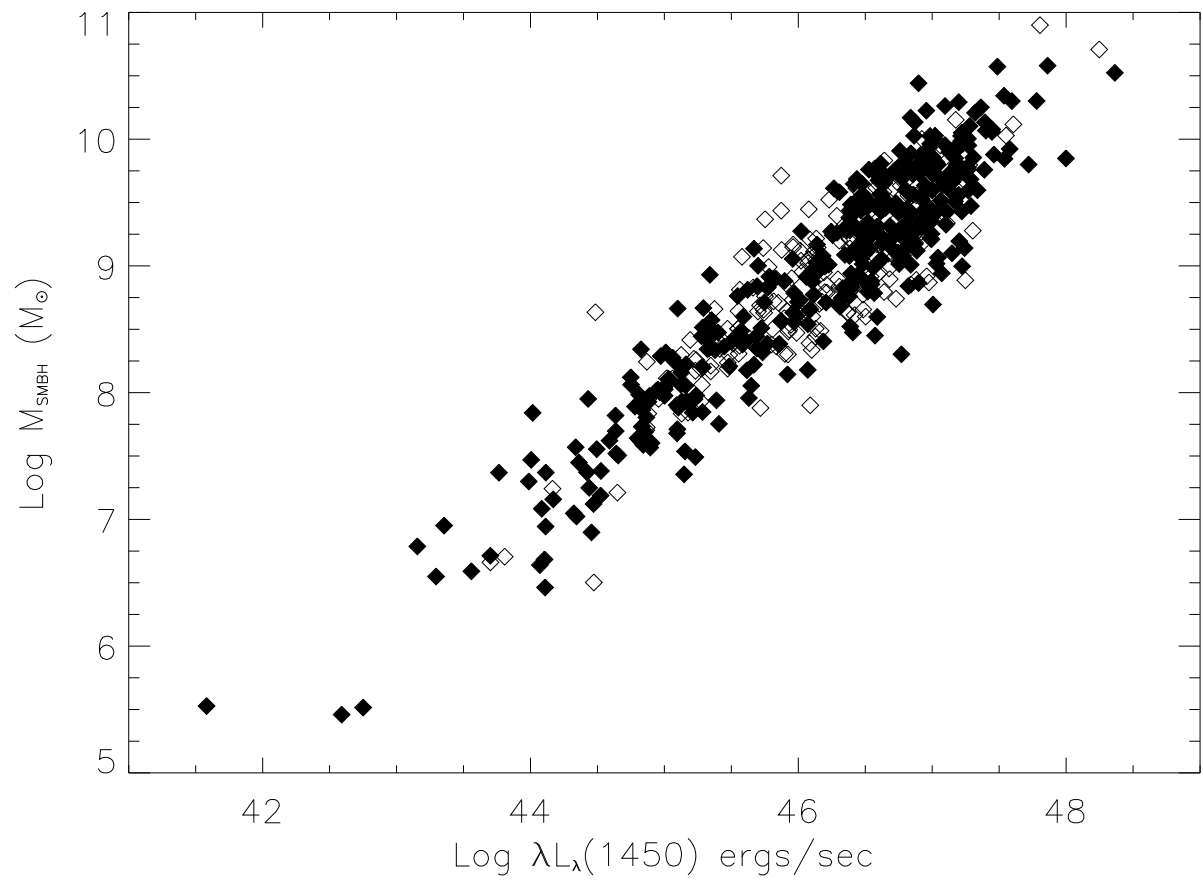


FIG. 7.— Continuum luminosity versus SMBH mass. There is a very strong correlation with little scatter. Symbols as in Fig. 6.

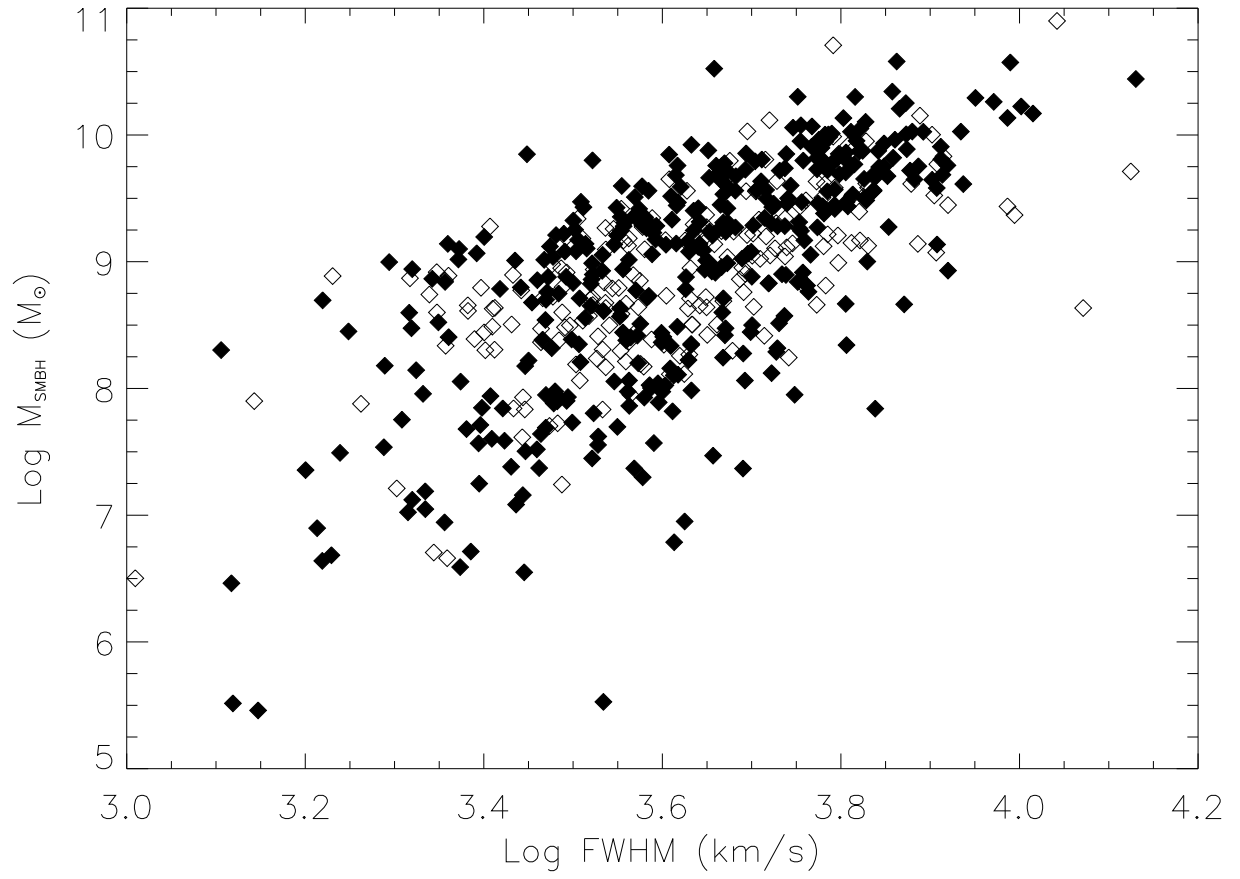


FIG. 8.— The FWHM of C IV versus SMBH mass. A trend is seen, but with a large amount of scatter. Symbols as in Fig. 6.

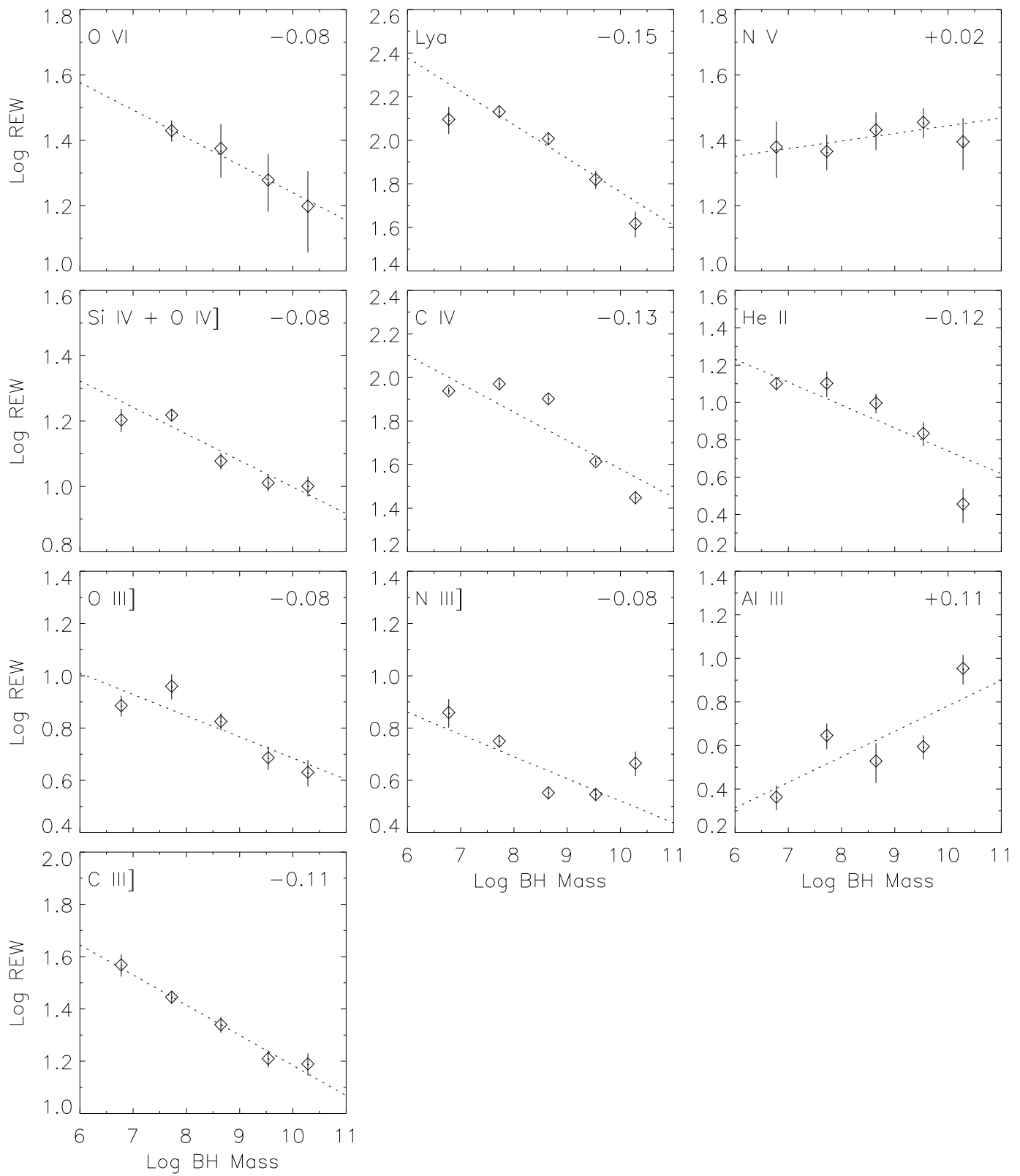


FIG. 9.— Emission line equivalent widths as a function of SMBH mass. We calculated linear fits to the EWs for the entire SMBH mass range using a chi-square minimization routine (dotted lines). The slopes of these fits are given in the upper right hand corner of each plot.

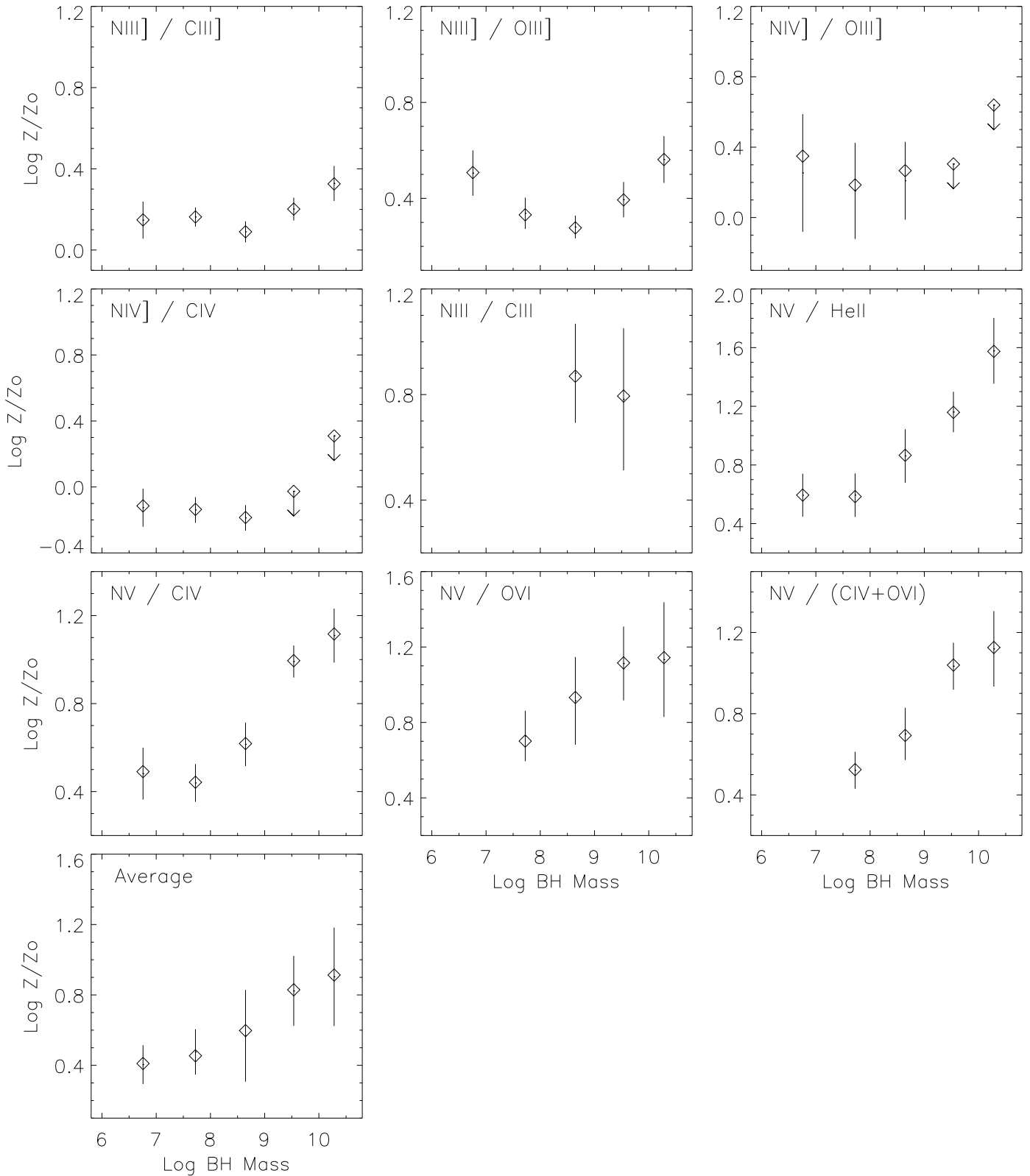


FIG. 10.— Metallicities derived from comparisons of different line ratio diagnostics to theoretical results from Figure 5 in Hamann et al. (2002) are shown as a function of SMBH mass. The average includes  $\text{N III]/C III]}$ ,  $\text{N III]/O III]}$ ,  $\text{N V/C IV]}$ , and  $\text{N V/O VI]}$ .

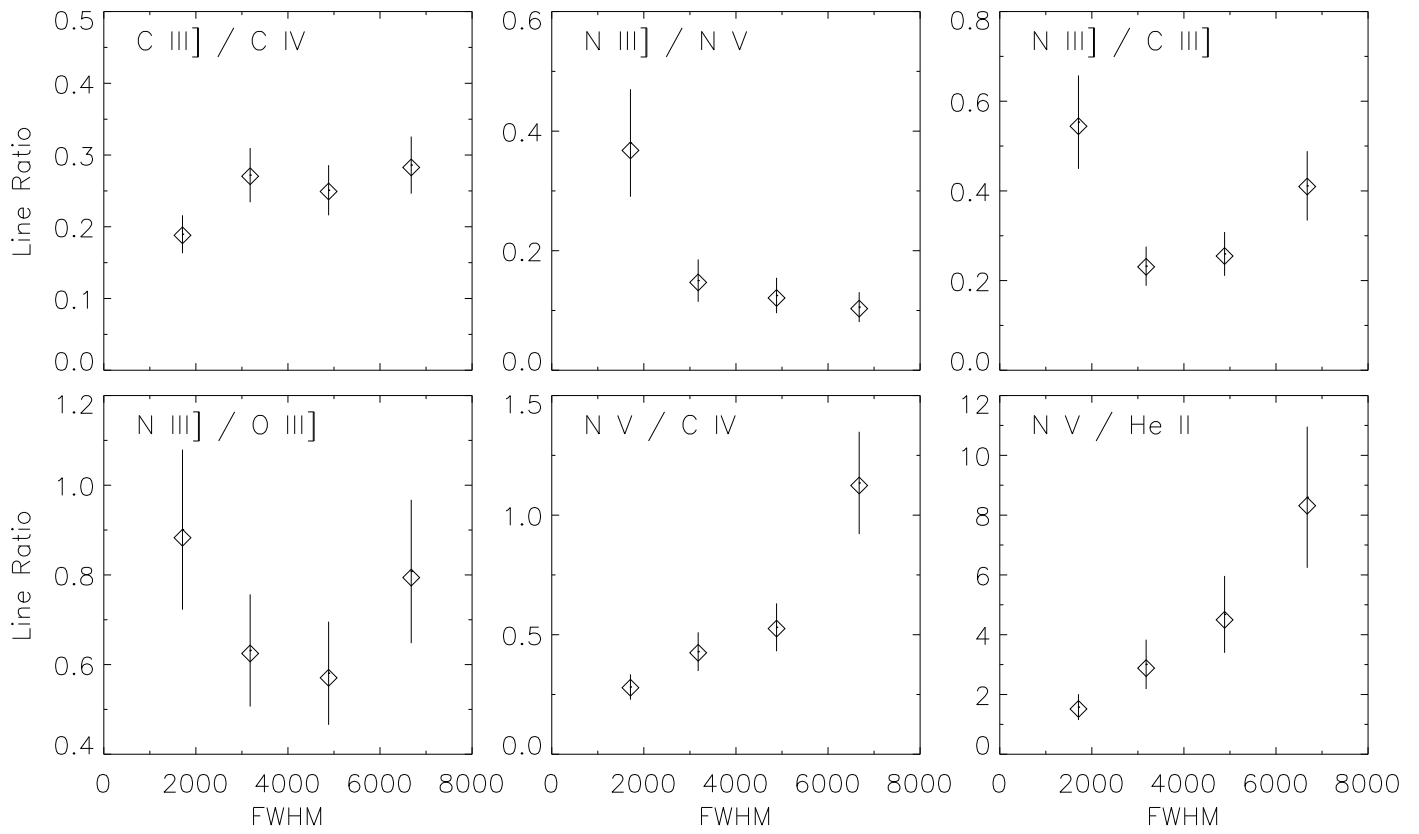


FIG. 11.— Emission line ratios are shown as a function of the FWHM of C IV.

TABLE 2  
EMISSION LINE DATA

Line	$10^6 M_{\odot}$			$10^7 M_{\odot}$			$10^8 M_{\odot}$			$10^9 M_{\odot}$			$10^{10} M_{\odot}$		
	Flux/Ly $\alpha$	REW <sup>a</sup>	FWHM <sup>b</sup>	Flux/Ly $\alpha$	REW <sup>a</sup>	FWHM <sup>b</sup>	Flux/Ly $\alpha$	REW <sup>a</sup>	FWHM <sup>b</sup>	Flux/Ly $\alpha$	REW <sup>a</sup>	FWHM <sup>b</sup>	Flux/Ly $\alpha$	REW <sup>a</sup>	FWHM <sup>b</sup>
C III $\lambda$ 977	–	–	–	–	–	–	0.023	2	3830	0.027	2	3170	–	–	–
N III $\lambda$ 991	–	–	–	–	–	–	0.029	3	3830	0.030	2	3170	0.057	2	3350
O VI $\lambda$ 1035	–	–	–	0.207	27	5800	0.242	24	4900	0.299	19	5700	0.396	16	8600
Ly $\alpha$ $\lambda$ 1216	1.000	125	1500	1.000	135	2500	1.000	102	3000	1.000	66	3800	1.000	42	6700
N V $\lambda$ 1240	0.191	24	2100	0.171	23	3100	0.264	27	3800	0.430	29	4700	0.597	25	6500
Si II $\lambda$ 1263	0.010	1	3070	0.012	2	3860	0.022	2	5010	0.026	2	4450	0.047	2	5340
O I $\lambda$ 1303	0.027	4	2000	0.027	4	4110	0.044	5	4650	0.052	4	4600	0.087	4	6320
C II $\lambda$ 1335	0.029	4	4140	0.015	2	3170	0.019	2	5380	0.027	2	4290	0.038	2	4360
Si IV + O IV]	0.113	16	4240	0.108	17	5340	0.102	12	5890	0.133	11	6340	0.205	10	7250
N IV] $\lambda$ 1486	0.019	3	2100	0.015	2	3100	0.014	2	3800	0.016 <sup>u</sup>	1 <sup>u</sup>	4700	0.033 <sup>u</sup>	2 <sup>u</sup>	6500
C IV $\lambda$ 1549	0.556	87	2100	0.547	94	3100	0.597	80	3800	0.462	41	4700	0.500	28	6500
He II $\lambda$ 1640	0.076	13	2300	0.070	13	4200	0.069	10	4300	0.071	7	6500	0.047	3	6800
O III] $\lambda$ 1665	0.046	8	2000	0.049	9	3200	0.046	7	3800	0.049	5	5000	0.068	4	6300
N III] $\lambda$ 1751	0.041	7	2100	0.029	6	3100	0.023	4	3800	0.033	4	4700	0.069	5	6500
Al III $\lambda$ 1859	0.012	2	2050	0.021	4	3460	0.020	3	3630	0.034	4	4430	0.122	9	6690
Si III] $\lambda$ 1892	0.023	4	2050	0.007	1	3460	0.007	1	3630	0.008	1	4430	0.010	1	6690
C III] $\lambda$ 1909	0.192	37	2300	0.130	28	3800	0.125	22	4200	0.135	16	6800	0.203	16	6700

<sup>a</sup>In units of Å

<sup>b</sup>In units of km s<sup>-1</sup>

<sup>u</sup>Upper limit for N IV